Article:
Zeng, M, Kim, Y-Y orcid.org/0000-0002-8503-4554, Anduix-Canto, C et al. (5 more authors) (2018) Confinement generates single-crystal aragonite rods at room temperature. Proceedings of the National Academy of Sciences, 115 (30). pp. 7670-7675. ISSN 0027-8424

https://doi.org/10.1073/pnas.1718926115

Confinement Generates Single-Crystal Aragonite Rods at Room Temperature

Short title: Confinement creates single-crystal aragonite rods

Muling Zeng[1,2], Yi-Yeoun Kim[1], Clara Anduix-Canto[1], Carlos Frontera[3], David Laundy[4], Nikil Kapur,[5] Hugo Christenson[2], and Fiona C. Meldrum[1]*

1. Dr. Muling Zeng, Dr.Yi-Yeoun Kim, Miss Clara Anduix-Canto and Prof. Fiona C. Meldrum
School of Chemistry, University of Leeds, Woodhouse Lane, Leeds, LS2 9JT, United Kingdom.
2. Dr. Muling Zeng and Prof. Hugo K. Christenson
School of Physics and Astronomy, University of Leeds, Woodhouse Lane, Leeds, LS2 9JT, United Kingdom
3. Dr Carlos Frontera
Institut de Ciencia de Materials de Barcelona, ICMAB-CSIC, 08290, Barcelona, Spain
4. Dr. David Laundy
Diamond Light Source, Didcot, Oxfordshire, OX11 0DE, UK
5. Prof Nikil Kapur
School of Mechanical Engineering, University of Leeds, Woodhouse Lane, Leeds, LS2 9JT, United Kingdom.

Corresponding authors: Prof Fiona Meldrum, f.meldrum@leeds.ac.uk, +44 113 3436414

PHYSICAL SCIENCES: Applied Physical Sciences

Abstract

The topic of calcite and aragonite polymorphism attracts enormous interest from fields including biomineralization and paleogeochemistry. While aragonite is only slightly less thermodynamically stable than calcite under ambient conditions, it typically only forms as a minor product in additive-free solutions at room temperature. Yet aragonite is an abundant biomineral, and certain organisms can selectively generate calcite and aragonite. This fascinating behavior has been the focus of decades of research, where this has been driven by a search for specific organic macromolecules that can generate these polymorphs. However, despite these efforts, we still have a poor understanding of how organisms achieve such selectivity. In this work, we consider an alternative possibility and explore whether the confined volumes in which all biomineralization occurs could also influence polymorph. Calcium carbonate was precipitated within the cylindrical pores of track-etched membranes, where these enabled us to systematically investigate the relationship between the membrane pore diameter and polymorph formation. Aragonite was obtained in increasing quantities as the pore size was reduced, such that oriented single crystals of aragonite were the sole product from additive-free solutions in 25 nm pores and significant quantities of aragonite formed in pores as large as 200 nm in the presence of low concentrations of magnesium and sulfate ions. This effect can be attributed to the effect of the pore size on the ion distribution, which becomes of increasing importance in small pores. These intriguing results suggest that organisms may exploit confinement effects to gain control over crystal polymorph.

Keywords: calcium carbonate, biomineralization, bio-inspired, biomimetic, track-etch membrane

Significance Statement

Calcium carbonate is a widespread compound, whose two common crystalline forms, calcite and aragonite, are important biominerals. Although aragonite is only marginally less stable than calcite under ambient conditions, it usually only crystallizes from solution at high temperatures or in the presence of magnesium ions. Yet organisms readily form both calcite and aragonite biominerals, a capacity usually attributed to the action of specific organic macromolecules. By investigating calcium carbonate precipitation in submicron pores, we here show that aragonite is promoted in confinement and that pure aragonite crystallizes in nanoscale pores in the absence of any additives. This is of great significance to biomineralization processes, which invariably occur in small volumes, and suggests that organisms may exploit confinement effects to control polymorph.

\body

Introduction

Biominerals provide a wonderful demonstration of the extent to which crystallization processes may be controlled.(1) However, while many of the general strategies that organisms use to control biomineralisation are known,(2) the mechanisms used to achieve control over polymorph remain unclear. From the outset of the field of biomineralization, researchers have isolated proteins entrapped within calcite and aragonite biominerals, with the expectation that these would enable polymorph control. However, despite a few isolated reports,(3) it appears that the mechanism is not so simple. There are also few examples of synthetic organic additives which induce aragonite precipitation at room temperature in the absence of magnesium ions.(4-6)

Nevertheless, there is a general strategy that reproducibly generates aragonite in the presence of organic additives: insoluble organic matrices containing soluble additives. Aragonite has been precipitated within cross-linked collagen films in the presence of poly(aspartic acid) and poly(glutamic acid),(7) and within re-acetylated chitosan thin films(8) and poly(vinyl alcohol) (PVA) matrices in the presence of poly(acrylic acid) (PAA).(9, 10) A more elaborate scaffold mimicking the organic matrix in which nacre forms was also created from β-chitin, silk-fibroin and macromolecules extracted from the aragonitic or calcitic layers of a mollusk; aragonite or calcite precipitated according to whether the macromolecules had been extracted from the aragonite or calcite biomineral, respectively.(11) Finally, the acidic matrix protein Pif promoted aragonite precipitation between a chitin membrane and glass slide.(12)

Common to all of the above systems is that the crystals form in defined micro-environments rather than in bulk solution, which is a feature that is intrinsic to all biomineralization processes. However, their complexity makes it difficult to investigate the factors that give rise to aragonite

formation, and the role played by confinement. The work described here employs a simple system – crystallization within the cylindrical pores of track-etched membranes – to systematically investigate how confinement influences calcium carbonate polymorph. Our data show that aragonite forms in increasing quantities as the pore size decreases, and that low concentrations of magnesium and sulfate ions support the formation of pure aragonite in larger pore sizes than under additive-free conditions. Magnesium and sulfate ions are significant components of the seawater in which many biomineralizing organisms live and promote aragonite formation.(13-15) It would hence be surprising if these ions do not contribute to aragonite formation in vivo.(16)

That significant quantities of aragonite are formed in pores as large as 200 nm when magnesium and sulfate ions^{-} are present is also of direct relevance to calcium carbonate biomineralization, where organisms such as mollusks and coccoliths can generate nano-sized $CaCO_3$; pteropods form beautiful shells comprising curved aragonite nanofibers 50-500 nm thick,(17) while holococcoliths comprise nano-sized calcite crystallites.(18) Our results therefore suggest that the privileged environments in which biominerals form may play a key role in controlling crystallization, where they may act in combination with organic macromolecules and inorganic ions to enable polymorph selection. They are also of significance to naturally-occurring microporous geological materials such as shales and clays,(19) where nanoscale pores can support precipitation reactions that do not occur in bulk.(20)

Results

Experiments were initially performed in bulk solution to identify the SO_4^{2-} and Mg^{2+} concentrations that promote low levels of aragonite. These biologically-relevant conditions were then used to determine if confinement can drive aragonite formation. The results obtained in the bulk solution experiments are summarized in Tables 1 and 2 and SI Appendix, Figure S1,

where the polymorphs present were quantified using powder XRD. Additional characterization was carried out using scanning electron microscopy (SEM) and Raman microscopy (SI Appendix, Figure S2) and typical morphologies for magnesian calcite, aragonite and vaterite were observed in all cases. Calcite formed in additive-free solutions at $[Ca^{2+}] = [CO_3^{2-}] = 1.5$ mM, while addition of magnesium at $[Ca^{2+}]$: $[Mg^{2+}]$ = 1:1 gave a very small increase in aragonite to levels of 2 %. In keeping with the literature, addition of SO_4^{2-} enhanced the ability of Mg^{2+} to promote aragonite formation at low supersaturations, such that 7 % aragonite formed at $[Ca^{2+}]$: $[Mg^{2+}]$: $[SO_4^{2-}]$ = 1: 2: 1.(15) A clear effect of the solution supersaturation was also seen such that at $[Ca^{2+}]$: $[Mg^{2+}]$: $[SO_4^{2-}]$ = 1: 2: 1, 11 % aragonite formed at $[Ca^{2+}] = [CO_3^{2-}] =$ 0.75 mM, 7 % at $[Ca^{2+}] = [CO_3^{2-}] = 1.5$ mM and none at $[Ca^{2+}] = [CO_3^{2-}] = 2.5$ mM. (Table 2 and SI Appendix, Figure S1).

Calcium carbonate was then precipitated within track-etched membranes with 1200, 800, 200, 50 and 25 nm pores. Membranes were placed between two half U-tube arms, one which was filled with a solution of $CaCl_2$ and $MgCl_2$, and the other with a solution of Na_2CO_3 and Na_2SO_4.(21) Counter diffusion then leads to $CaCO_3$ precipitation within the pores. No pressure is applied to the system and the pressure within the pores is identical to that in the reservoirs. As typical results from our "standard" experimental conditions of $[Ca^{2+}] = [CO_3^{2-}] = 1.5$ mM and $[Ca^{2+}]$: $[Mg^{2+}]$: $[SO_4^{2-}]$ = 1: 2: 1, rod-shaped crystals with lengths of up to 15 μm (comparable to the membrane thickness of ≈ 20 μm) formed in the membrane pores (Figures 1 and SI Appendix, Figure S3). Rods isolated from the smaller pores tended to be shorter, likely due to breakage of the more fragile, thinner rods during isolation from the membrane.

Investigation of the effects of confinement on the polymorphs of the intra-membrane crystals precipitated under these standard conditions yielded fascinating results. Powder XRD showed that the crystals formed within the 1200 nm pores were almost entirely calcite (97 % calcite and

3 % aragonite), in common with bulk solution, while the crystals formed in the 800 nm pores were 81 % calcite and 19 % aragonite (Table 1, Figure 2 and SI Appendix, Figure S4). Further reduction in the pore size to 200 nm significantly increased the proportion of aragonite to 69 %. Polymorph analysis of the crystals formed in smaller pores (50 and 25 nm) was conducted using synchrotron micro-beam XRD and electron diffraction as too little material was available for laboratory PXRD, and aragonite was the only polymorph identified in the 50 nm and 25 nm pores (Figure 2). Aragonite was therefore promoted in pores of size 800 nm and smaller in the presence of both Mg^{2+} and SO_4^{2-}.

Individual rods grown in the 200, 50 and 25 nm pores were also investigated using selected area electron diffraction (SAED) to determine their single crystal/ polycrystalline structures and to identify any preferential orientation (larger rods were too thick for SAED) (Figure 3). At least 17 rods were characterized in each case. The aragonite crystals grown in the 200 nm pores were clearly polycrystalline and showed no preferential orientation. Those in the 50 nm pores, in contrast, were almost single crystals, while the 25 nm rods were indistinguishable from single crystals. These aragonite crystals were also preferentially oriented with their crystallographic c-direction parallel to the pore axis, such that 50 % and 100 % of rods in the 50 and 25 nm pores were oriented in this way. Further representative data and analysis of the SAED patterns are given in SI Appendix, Figures S5 and S6. It is noted that some crystals also precipitate on the membrane surface, providing an internal "control". In all cases these were principally calcite, with a small percentage of vaterite.

The effect of the Ca^{2+} concentration was then studied by varying this parameter while holding the $[Ca^{2+}]$: $[Mg^{2+}]$: $[SO_4^{2-}]$ ratio at 1: 2: 1. (Table 2, Figure 4 and SI Appendix, Figure S4). Comparable levels of aragonite were observed at $[Ca^{2+}] = [CO_3^{2-}] = 0.75$ mM as under the standard conditions in the 200 nm ($\approx$ 70 %) and 50 nm pores (100 %), but both pore sizes now

supported the formation of single crystals (Figure 4). All of the aragonite rods in the 50 nm pores were also c-oriented as compared with 50 % under the standard conditions. The rods produced at [Ca^{2+}] = 2.5 mM, in contrast, were only 2 % aragonite in the 200 nm pores and 64 % in the 50 nm pores, where only 50 % of the latter were c-oriented. These experiments thus follow the same trend as the bulk experiments with aragonite being favored at lower supersaturations.

Experiments were also conducted to explore the individual effects of Mg^{2+} and SO_4^{2-} ions (Table 1 and SI Appendix, Figure S4). Looking first at the effect of SO_4^{2-}, its elimination from the "standard" conditions caused a reduction in the amount of aragonite from 7 % to 2 % in bulk solution (SI Appendix, Figure S1). In the equivalent membrane-based experiments, little aragonite formed in the 1200 and 800 nm pores, while 32 % aragonite formed in the 200 nm pores, as compared with 69 % under the "standard conditions". With further reduction in the pore size to 50 nm all of the particles characterized approached single crystal aragonite (SI Appendix, Figure S6). Single crystal rods of aragonite formed in the most confined environment of the 25 nm pores (Figure 5 and SI Appendix, Figure S5). Therefore, when just Mg^{2+} were present, it was not until the pores decreased in size to 200 nm that a change in the calcite/ aragonite ratio was observed.

Finally, experiments were conducted in the absence of both Mg^{2+} and SO_4^{2-}. Very little aragonite formed in the 1200 and 800 nm pores, just 8 % in the 200 nm pores (Table 1 and SI Appendix Figure S4) and a significant increase to 47 % was recorded in the 50 nm pores. (SI Appendix, Figure S7) Precipitation within the 25 nm pores, however, yielded a most unexpected result – aragonite single crystals formed in the absence of any additives in these very small pores (Figure 5 and SI Appendix, Figure S5). All of the rods examined were

aragonite and ≈ 90 % were oriented with the crystallographic c-axis parallel to the long axis of the pore.

Discussion

We have previously shown that track-etched membranes provide a versatile means of studying the effects of confinement on the polymorph, orientation and single crystal/ polycrystalline structure of inorganic crystals.(21-26) Briefly reviewing these studies, our early work employed pores as small as 200 nm, and used low temperatures and 100 mM $CaCl_2$ and Na_2CO_3 solutions to generate single crystals of calcite via an amorphous calcium carbonate (ACC) precursor phase.(22, 23) A later study induced $CaCO_3$ precipitation in 200 nm pores in the absence of ACC using the ammonia diffusion method and 10 mM $CaCl_2$ solutions.(21) There, membranes were sourced from different manufacturers and generated either single crystal calcite or vaterite rods under conditions where calcite precipitated in bulk solution. That article also provided a detailed characterization of the surface chemistry and topography of the membranes using methods including IR spectroscopy, X-ray photoelectron spectroscopy (XPS), BET and AFM, and showed that the vast majority of the carbon atoms on the surfaces of the membranes were bound in aryl rings and aliphatic chains as expected for polycarbonate. Finally, we showed that the polyelectrolyte PAA can facilitate infiltration of ACC into 100 nm pores, leading to the generation of high-aspect ratio calcite single crystals.(26) It is also noted that there is one report of the precipitation of aragonite nanoparticles within the peptide-functionalized pores of anodic alumina membranes.(27) However, as such membranes gradually dissolve in alkaline solutions, releasing aluminium complexes,(28) the formation of aragonite cannot be clearly attributed to confinement effects.

Our current results demonstrate that confinement can promote the formation of aragonite such that 47 % and 100 % of the crystals precipitated in 50 nm and 25 nm pores were aragonite under

additive-free conditions. This effect is enhanced in the presence of low concentrations of Mg^{2+} and SO_4^{2-}, where 8 % of the crystals formed in 200 nm pores under conditions $[Ca^{2+}] = [CO_3^{2-}]$ = 1.5 mM were aragonite as compared with 32 % when Mg^{2+} ions were also present. Addition of further Mg^{2+} and SO_4^{2-} enhanced this effect yet further, delivering 69 % aragonite.

What then are the origins of these effects? Calcite/aragonite polymorphism is a complex problem that has challenged researchers for decades. The production of these mineral phases from solution is dependent on kinetics as well as thermodynamics,(29) and thus on variables including temperature, supersaturation and the presence of additives. While aragonite is only slightly less thermodynamically stable than calcite at room temperature, it typically only appears as a minor product on precipitation from additive-free solutions at room temperature. The proportion of aragonite increases significantly as the temperature is raised towards 100 ^oC, even though its stability with respect to calcite does not increase in this temperature regime,(30, 31) where this is indicative of changes in the relative rates of nucleation and growth. For both polymorphs, nucleation and growth processes are obstructed by water molecules solvating the cations, which may be more significant for the denser aragonite structure.(32) Environments which offer reduced levels of hydration or facilitate dehydration (such as higher temperatures or solutions with decreasing dielectric constants) may thus favor aragonite.(33, 34)

Given that aragonite is so difficult to precipitate as a major product in bulk solution under additive-free conditions at room temperature it is striking that many systems that offer localized environments including collagen(7) and silica gels,(35) and polymer thin films(8, 10) can deliver high proportions of aragonite. An apparently universal effect of confinement is that it increases induction times; as nucleation is a stochastic phenomenon, a reduction in the number of available ions, and the elimination of advection and convection reduces the probability of nucleation.(36) This is most significant for the thermodynamically favored phase (here calcite)

and leads to the formation and stabilization of metastable phases as precursors to the final phase.(37-47) However, this effect cannot explain the generation of aragonite as it is seldom seen as a precursor to calcite.(48)

Confinement also affects ion transport such that diffusion is the sole mechanism in small pores. The diffusion coefficients of water and ion transport can vary in small pores, but this only occurs in pores of a few nanometers in diameter.(49) Analysis of calcium carbonate precipitation within silica gels has demonstrated that diffusion leads to an evolving supersaturation profile, and crystals with different morphologies and polymorphs form at different times and locations in the gel. These are in turn associated with different threshold supersaturations, which are defined by the rate of change of supersaturation.(35, 50)

The possibility that comparable effects give rise to aragonite formation in the membrane pores was therefore explored. Diffusion of ions through the membrane pores was modelled using the diffusion equation to determine how the supersaturation profile changed over time. Boundary conditions along the pore wall were chosen to reflect no ion transport across the wall with no other ion-surface interactions present. This showed that the calcium and carbonate solutions were fully mixed in under 0.1 sec (SI Appendix, Figure S8), where mixing is rapid due to the short (20 μm) length of the pore. The formation of aragonite cannot therefore be attributed to an evolving supersaturation profile.

None of the above factors takes into account the potential influence of the membrane surface on crystal nucleation. We therefore analyzed our data in light of this possibility to explore the relationship between the aragonite fraction and the pore diameter. A graph of the aragonite fraction versus the inverse of the pore diameter (Figure 6) reveals a roughly linear relationship between these quantities. Admittedly, the number of data points is small and we make no

quantitative claims about the significance of the slopes. Nevertheless, a linear relationship is to be expected if the number of aragonite nucleation sites is proportional to the surface area (d^2), while the amount of $CaCO_3$ is proportional to volume (d^3) and the crystal growth rate is constant. Thus, as the surface increases in importance relative to the bulk with the degree of confinement, the proportion of aragonite increases.

It is also noted that the distribution of ions adjacent to a charged membrane surface can differ significantly in a membrane pore as compared to a planar surface. This has been discussed in several theoretical/simulation papers,(51-53) and the results show that there may be a non-monotonic ion concentration profile away from the pore surface, particularly for divalent ions, unlike the case for a planar surface. The pores in track-etch membranes are negatively charged independent of the pore diameter,(54) and under some circumstances an enhanced co-ion (carbonate ion) concentration towards the centre of the pore may result. Such changes in ion concentration may influence polymorph formation, where it has been suggested that higher concentrations of carbonate promote aragonite formation.(55) This is further supported by numerical simulations which predict lower ion activity coefficients adjacent to a charged membrane surface, and thus preferential formation of crystals in the center of pores.(56)

Unfortunately, it is not currently possible to measure the ionic profiles next to a charged surface in submicron pores. Theory/ simulations therefore provide our only window into these effects. Our results hence show that the formation of aragonite in small volumes is intimately linked to the properties of the confining surface, where a surface-induced alteration of the local ionic environment may stabilize aragonite with respect to calcite. That calcite is precipitated on the outer surfaces of the membranes at the same time that aragonite precipitates within the pores additionally indicates that the highly controlled environments of the membrane pores – in which

diffusion dominates as the transport mechanism – are vital to the generation of local solution conditions that favor aragonite over calcite.

Conclusions

This study demonstrates that confinement can promote the formation of aragonite. Oriented single crystals of aragonite formed in 25 nm pores of track-etched membranes, while low concentrations of Mg^{2+} and SO_4^{2-} ions supported the formation of significant quantities of aragonite in pores as large as 200 nm. Analysis of ion diffusion through the pores and determination of the relationship between the pore diameter and polymorph formation suggests that this behavior derives from the modified ionic environment adjacent to the pore surfaces. These results are of particular significance to calcium carbonate biomineralization, which invariably occurs in privileged environments bound by organic matrices.(1) Confinement effects may enhance the influence of such organic frameworks on crystallization, enabling organisms to achieve superior control over characteristics such as polymorph or orientation. Well-defined confined systems including liposomes,(41) and microfluidic devices(57-60) therefore provide unique opportunities for studying such effects, and could ultimately enable us to build an enhanced understanding of the factors which govern calcite/aragonite polymorphism.

Materials and Methods

Full details of the materials and methods are given in the SI Appendix. Briefly, $CaCO_3$ was precipitated within porous track-etched membranes by placing a membrane between two half U-tube arms, and filling one with a solution of $CaCl_2$ and $MgCl_2$, and the other with a solution of Na_2CO_3 and Na_2SO_4. The precipitated $CaCO_3$ was then isolated by dissolution of the membranes in dichloromethane. Experiments were performed in the presence and absence of Mg^{2+} and SO_4^{2-} ions, and were compared with control experiments performed in bulk solution. The crystals were characterized using techniques including TEM, electron diffraction, powder XRD and Raman spectroscopy.

Acknowledgements

We would like to thank the Engineering and Physical Sciences Research Council (EPSRC) for funding this work under grants EP/N002423/1 (MZ, YYK, HKC, FCM) and EP/J018589/1 (YYK, FCM), and the Leverhulme Trust for funding under a Research Project Grant (YYK, NK, FCM). We also thank Diamond Light Source for provision of beamtime (proposal MT14790-1), Oriol Vallcorba Vall from ALBA Synchrotron for his help in μ-XRD analysis and Michael Ward (Leeds University) for his help in TEM analysis.

References

1. Lowenstam HA & Weiner S (1989) On Biomineralization (Oxford University Press, New York).
2. Meldrum FC & Colfen H (2008) Controlling Mineral Morphologies and Structures in Biological and Synthetic Systems. Chem. Revs. 108(11):4332-4432.
3. Belcher AM, et al. (1996) Control of crystal phase switching and orientation by soluble mollusc-shell proteins. Nature 381(6577):56-58.
4. Litvin AL, Valiyaveettil S, Kaplan DL, & Mann S (1997) Template-directed synthesis of aragonite under supramolecular hydrogen-bonded Langmuir monolayers. Adv. Mater. 9(2):124-127.
5. Nassif N, et al. (2005) Synthesis of stable aragonite superstructures by a biomimetic crystallization pathway. Angew. Chem. Int. Ed. 44(37):6004-6009.
6. Willinger MG, et al. (2015) Structural evolution of aragonite superstructures obtained in the presence of the siderophore deferoxamine. Crystengcomm 17(21):3927-3935.
7. Falini G, Fermani S, Gazzano M, & Ripamonti A (1998) Oriented crystallization of vaterite in collagenous matrices. Chem.-Eur. J. 4(6):1048-1052.
8. Munro NH & McGrath KM (2012) Biomimetic approach to forming chitin/aragonite composites. Chem. Commun. 48(39):4716-4718.
9. Hosoda N, Sugawara A, & Kato T (2003) Template effect of poly(vinyl alcohol) for selective formation of aragonite and vaterite $CaCO_3$ thin films. Macromols. 36(17):6449-6452.
10. Kajiyama S, Nishimura T, Sakamoto T, & Kato T (2014) Aragonite nanorods in calcium carbonate/polymer hybrids formed through self-organization processes from amorphous calcium carbonate solution. Small 10(8):1634-1641.
11. Falini G, Albeck S, Weiner S, & Addadi L (1996) Control of aragonite or calcite polymorphism by mollusk shell macromolecules. Science 271(5245):67-69.
12. Suzuki M, et al. (2009) An acidic matrix protein, Pif, as a key macromolecule for nacre formation. Science 325(5946):1388-1390.
13. Morse JW, Arvidson RS, & Luttge A (2007) Calcium carbonate formation and dissolution. Chem. Rev. 107(2):342-381.
14. Balthasar U & Cusack M (2015) Aragonite-calcite seas-Quantifying the gray area. Geology 43(2):99-102.
15. Bots P, Benning LG, Rickaby REM, & Shaw S (2011) The role of SO_4 in the switch from calcite to aragonite seas. Geology 39(4):331-334.
16. Bentov S, Brownlee C, & Erez J (2009) The role of seawater endocytosis in the biomineralization process in calcareous foraminifera. Proc. Natl. Acad. Sci. USA 106(51):21500-21504.
17. Zhang T, et al. (2011) Structure and Mechanical Properties of a Pteropod Shell Consisting of Interlocked Helical Aragonite Nanofibers. Angew. Chem. Int. Ed. 50(44):10361-10365.
18. Addadi L, Gal A, Faivre D, Scheffel A, & Weiner S (2016) Control of Biogenic Nanocrystal Formation in Biomineralization. Israel J. Chem. 56(4):227-241.
19. Wang YF (2014) Nanogeochemistry: Nanostructures, emergent properties and their control on geochemical reactions and mass transfers. Chem. Geol. 378:1-23.
20. Prasianakis NI, Curti E, Kosakowski G, Poonoosamy J, & Churakov SV (2017) Deciphering pore-level precipitation mechanisms. Sci Rep 7:9.
21. Schenk AS, Albarracin EJ, Kim YY, Ihli J, & Meldrum FC (2014) Confinement stabilises single crystal vaterite rods. Chem. Commun. 50(36):4729-4732.

22. Loste E & Meldrum FC (2001) Control of calcium carbonate morphology by transformation of an amorphous precursor in a constrained volume. Chem. Commun. (10):901-902.
23. Loste E, Park RJ, Warren J, & Meldrum FC (2004) Precipitation of calcium carbonate in confinement. Adv. Funct. Mater. 14(12):1211-1220.
24. Cantaert B, Beniash E, & Meldrum FC (2013) Nanoscale Confinement Controls the Crystallization of Calcium Phosphate: Relevance to Bone Formation. Chem.-Eur. J. 19(44):14918-14924.
25. Cantaert B, Beniash E, & Meldrum FC (2013) The role of poly(aspartic acid) in the precipitation of calcium phosphate in confinement. J. Mater. Chem. B 1(48):6586-6595.
26. Kim YY, et al. (2011) Capillarity creates single-crystal calcite nanowires from amorphous calcium carbonate. Angew. Chem. Int. Ed. 50(52):12572-12577.
27. Lee J & Morse JW (2010) Influences of alkalinity and pCO_2 on $CaCO_3$ nucleation from estimated Cretaceous composition seawater representative of "calcite seas". Geology 38(2):115–118.
28. Petukhov DI, Buldakov DA, Tishkin AA, Lukashin AV, & Eliseev AA (2017) Liquid permeation and chemical stability of anodic alumina membranes. Beilstein J. Nanotechnol. 8(561-570).
29. Gutjahr A, Dabringhaus H, & Lacmann R (1996) Studies of the growth and dissolution kinetics of the $CaCO_3$ polymorphs calcite and aragonite .1. Growth and dissolution rates in water. J. Cryst. Growth 158(3):296-309.
30. Wray JL & Daniels F (1957) Precipitation of calcite and aragonite. J. Am. Chem. Soc. 79(9):2031-2034.
31. Ogino T, Suzuki T, & Sawada K (1987) The formation and transformation mechanism of calcium carbonate in water. Geochim. Cosmochim. Acta 51(10):2757-2767.
32. Lippmann F (1973) Sedimentary carbonate materials (Springer-Verlag, Berlin).
33. Chen SF, Yu SH, Jiang J, Li FQ, & Liu YK (2006) Polymorph discrimination of $CaCO_3$ mineral in an ethanol/water solution: Formation of complex vaterite superstructures and aragonite rods. Chem. Mater. 18(1):115-122.
34. Lenders JJM, et al. (2012) High-Magnesian Calcite Mesocrystals: A Coordination Chemistry Approach. J. Am. Chem. Soc. 134(2):1367-1373.
35. FernandezDiaz L, Putnis A, Prieto M, & Putnis CV (1996) The role of magnesium in the crystallization of calcite and aragonite in a porous medium. J. Sediment. Res. 66(3):482-491.
36. Putnis A (2015) Transient Porosity Resulting from Fluid-Mineral Interaction and its Consequences. Pore-Scale Geochemical Processes, Reviews in Mineralogy & Geochemistry, eds Steefel CI, Emmanuel S, & Anovitz LM), Vol 80, pp 1-23.
37. Wang YW, Christenson HK, & Meldrum FC (2013) Confinement Leads to Control over Calcium Sulfate Polymorph. Adv. Funct. Mater. 23(45):5615-5623.
38. Stephens CJ, Ladden SF, Meldrum FC, & Christenson HK (2010) Amorphous calcium carbonate is stabilized in confinement. Adv. Funct. Mater. 20(13):2108-2115.
39. Jiang Q & Ward MD (2014) Crystallization under nanoscale confinement. Chem. Soc. Revs. 43(7):2066-2079.
40. Stephens CJ, Kim YY, Evans SD, Meldrum FC, & Christenson HK (2011) Early stages of crystallization of calcium carbonate revealed in picoliter droplets. J. Am. Chem. Soc. 133(14):5210-5213.
41. Tester CC, Whittaker ML, & Joester D (2014) Controlling nucleation in giant liposomes. Chem. Commun. 50(42):5619-5622.
42. Wang YW, Christenson HK, & Meldrum FC (2014) Confinement Increases the Lifetimes of Hydroxyapatite Precursors. Chem. Mater. 26(20):5830-5838.

43. Ihli J, et al. (2015) Precipitation of amorphous calcium oxalate in aqueous solution. Chem. Mater. 27(11):3999-4007.
44. Anduix-Canto C, et al. (2016) Effect of Nanoscale Confinement on the Crystallization of Potassium Ferrocyanide. Cryst. Growth Des. 16(9):5403-5411.
45. Wang YW, Zeng ML, Meldrum FC, & Christenson HK (2017) Using Confinement To Study the Crystallization Pathway of Calcium Carbonate. Cryst. Growth Des. 17(12):6787-6792.
46. Whittaker ML, Dove PM, & Joester D (2016) Nucleation on surfaces and in confinement. MRS Bulletin 41(5):388-392.
47. Hamilton BD, Ha JM, Hillmyer MA, & Ward MD (2012) Manipulating Crystal Growth and Polymorphism by Confinement in Nanoscale Crystallization Chambers. Acc. Chem. Res. 45(3):414-423.
48. Bots P, Benning LG, Rodriguez-Blanco JD, Roncal-Herrero T, & Shaw S (2012) Mechanistic insights into the crystallization of amorphous calcium carbonate (ACC). Cryst. Growth Des. 12(7):3806-3814.
49. Nishizawa M, Menon VP, & Martin CR (1995) Metal Nanotubule Membranes witrh Electrochemically Switchable Ion-Transport Selectivity. Science 268(5211):700-702.
50. Prieto M (2014) Nucleation and supersaturation in porous media (revisited). Mineral. Mag. 78(6):1437-1447.
51. Yeomans L, Feller SE, Sanchez E, & Lozada-Cassou M (1993) The structure of electrolytes in cylindrical pores. J. Chem. Phys. 83:1436-1450.
52. Vlachy V (2001) Ion-partitioning beteween charged capillaries and bulk electrolyte solution: an example of negative rejection. Langmuir 17:399-402.
53. Luksic M, Vlachy V, & Hribar-Lee B (2012) Modelling the ion-exchange equilibrium in nanoporous materials. Cond. Matter Phys. 15(2).
54. Diez LM, Villa FM, Gimenez AH, & Garcia FT (1989) Streaming Potentials of Some Polycarbonate Microporous Membranes when Bathed by LiCl, NaCl, $MgCl_2$, and $CaCl_2$ Aqueous Solutions. J. Coll. Int. Sci. 132(1):27-33.
55. Given RK & Wilkinson BH (1985) Kinetic control of morphology, compoisiton and mineralogy of abiotic sedimentary carbonates. J. Sed. Petrol. 55(1):109-119.
56. Murmann M, Kuhn M, Pape H, & Clauser C (2013) Numerical simulation of pore size dependent anhydrite precipitation in geothermal reservoirs. Energy Procedia 40:107-116.
57. Yashina A, Meldrum F, & deMello A (2012) Calcium carbonate polymorph control using droplet-based microfluidics. Biomicrofluidics 6(2).
58. Li S, Zeng M, Gaule T, McPherson MJ, & Meldrum FC (2017) Passive picoinjection enables controlled crystallization in a droplet microfluidic device. Small.
59. Kim Y-Y, et al. (2017) The effect of additives on the early stages of growth of calcite single crystals. Angew. Chem. Int. Ed. 56(39):11885-11890.
60. Bawazer LA, et al. (2016) Combinatorial microfluidic droplet engineering for biomimetic material synthesis. Sci. Adv. 2(10).

Table 1. Summary of the $CaCO_3$ polymorphs precipitated in bulk solution and within the TE membrane pores at the indicated reaction conditions. All data were obtained using laboratory PXRD with the exception of the 25 and 50 nm pores which were studied using synchrotron micro-beam XRD and electron diffraction (ED). A: Aragonite; C: Calcite; V: Vaterite.

Pore Size / Solution conditions	Bulk	1200 nm	800 nm	200 nm	50 nm	25 nm
$[Ca^{2+}] = [CO_3^{2-}] = 1.5$ mM $[Ca^{2+}] :[Mg^{2+}]:[SO_4^{2-}] = 1:2:1$ "standard" conditions	7% A 93% C 0% V	3% A 97% C 0% V	19% A 81% C 0% V	69% A 31% C 0% V Polycrystalline A	100% A ≈50% c-oriented Approaching single crystal A	100% A ≈100% c-oriented Single Crystal A
$[Ca^{2+}] = [CO_3^{2-}] = [Mg^{2+}] = 1.5$ mM No SO_4^{2-}	2% A 98% C 0% V	1% A 97% C 2% V	4% A 96% C 0% V	32% A 68% C 0% V	100% A ≈50% c-oriented Approaching single crystal A	100% A ≈80% c-oriented Single Crystal A
$[Ca^{2+}] = [CO_3^{2-}] = 1.5$ mM No Mg^{2+} or SO_4^{2-}	0% A 100% C 0% V	1% A 98% C 1% V	3% A 96% C 1% V	8 % A 92 % C 0 % V	47% A 53% C 0 % V Single Crystal A	100% A ≈90% c-oriented Single Crystal A

Table 2. Summary of the $CaCO_3$ polymorphs precipitated in bulk solution and within the TE membrane pores with varied supersaturations at the standard condition, $[Ca^{2+}]$: $[Mg^{2+}]$: $[SO_4^{2-}]$ = 1:2:1 . All data were obtained using laboratory PXRD with the exception of the 25 and 50 nm pores which were studied using synchrotron micro-beam XRD and electron diffraction (ED). A: Aragonite; C: Calcite; V: Vaterite.

Pore size	**$[Ca^{2+}] = [CO_3^{2-}] = 0.75$ mM $[Ca^{2+}]:[Mg^{2+}]:[SO_4^{2-}] = 1:2:1$**	**$[Ca^{2+}] = [CO_3^{2-}] = 1.5$ mM $[Ca^{2+}]:[Mg^{2+}]:[SO_4^{2-}] = 1:2:1$**	**$[Ca^{2+}] = [CO_3^{2-}] = 2.5$ mM $[Ca^{2+}]:[Mg^{2+}]:[SO_4^{2-}] = 1:2:1$**
Bulk	11% A; 89% C; 0% V	7% A; 93% C; 0% V	0% A; 71% C; 29% V
200 nm	72% A; 28% C; 0% V ≈100% in c-orientation Single Crystal	69% A; 31% C; 0% V Polycrystalline	2% A; 68% C; 30% V Polycrystalline
50 nm	100% A ≈100% in c-orientation Single Crystal	100% A ≈ 50% c-oriented Approaching single crystal	64% A; 36% V ≈ 50% c-oriented Approaching single crystal
25 nm	–	100% A ≈100% c-oriented Single Crystal	–

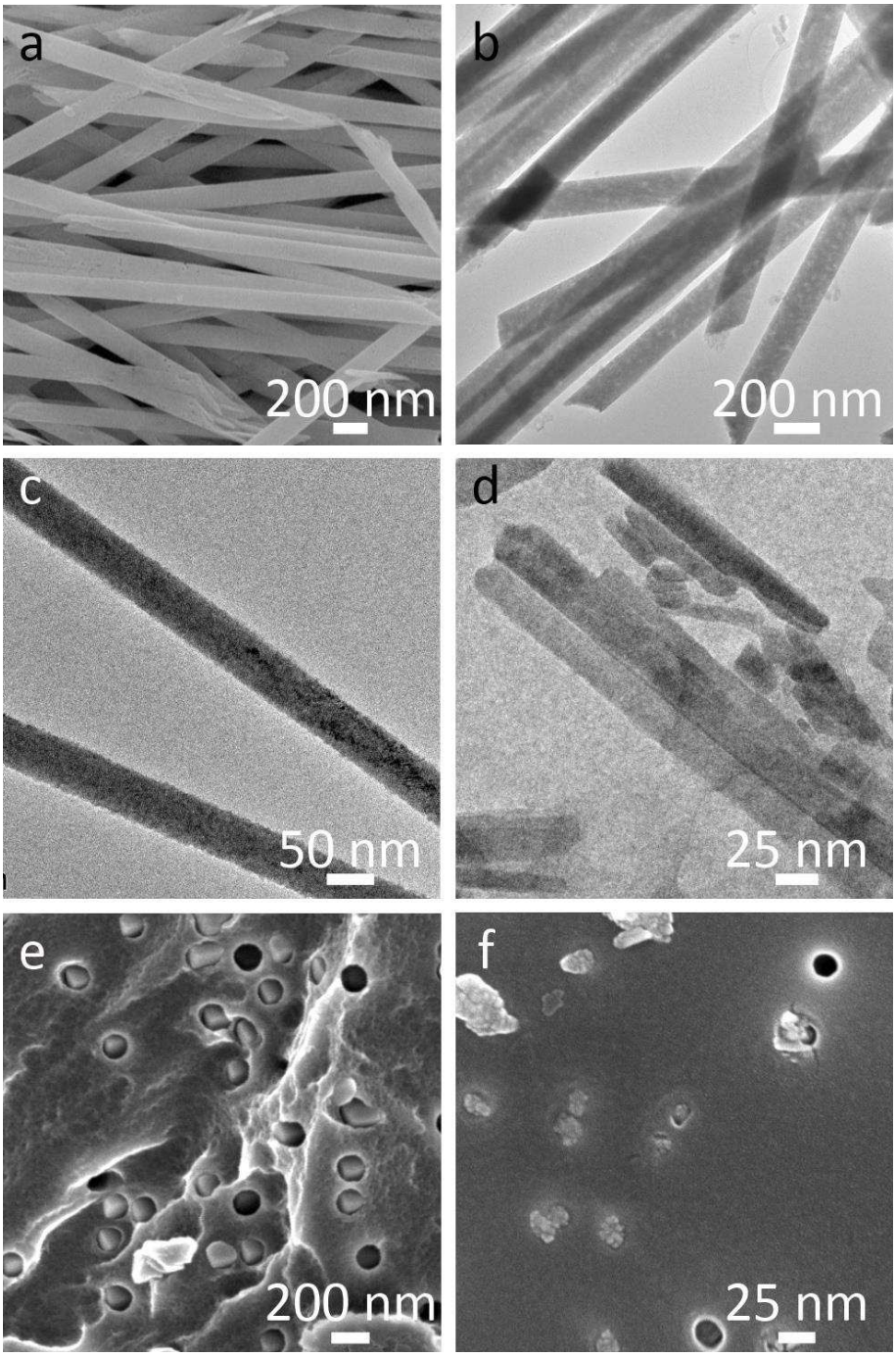

Figure 1. Calcium carbonate crystals precipitated within membrane pores under reaction conditions of $[Ca^{2+}] = [CO_3^{2-}] = 1.5$ mM and $[Ca^{2+}]: [Mg^{2+}]: [SO_4^{2-}] = 1: 2: 1$. (a-b) SEM and TEM images of crystal rods isolated from 200 nm pore membranes, (c-d) TEM images of the crystal rods isolated from 50 and 25 nm pore membranes, (e-f) SEM images of the anion-side of the membrane with 200 and 50 nm pores.

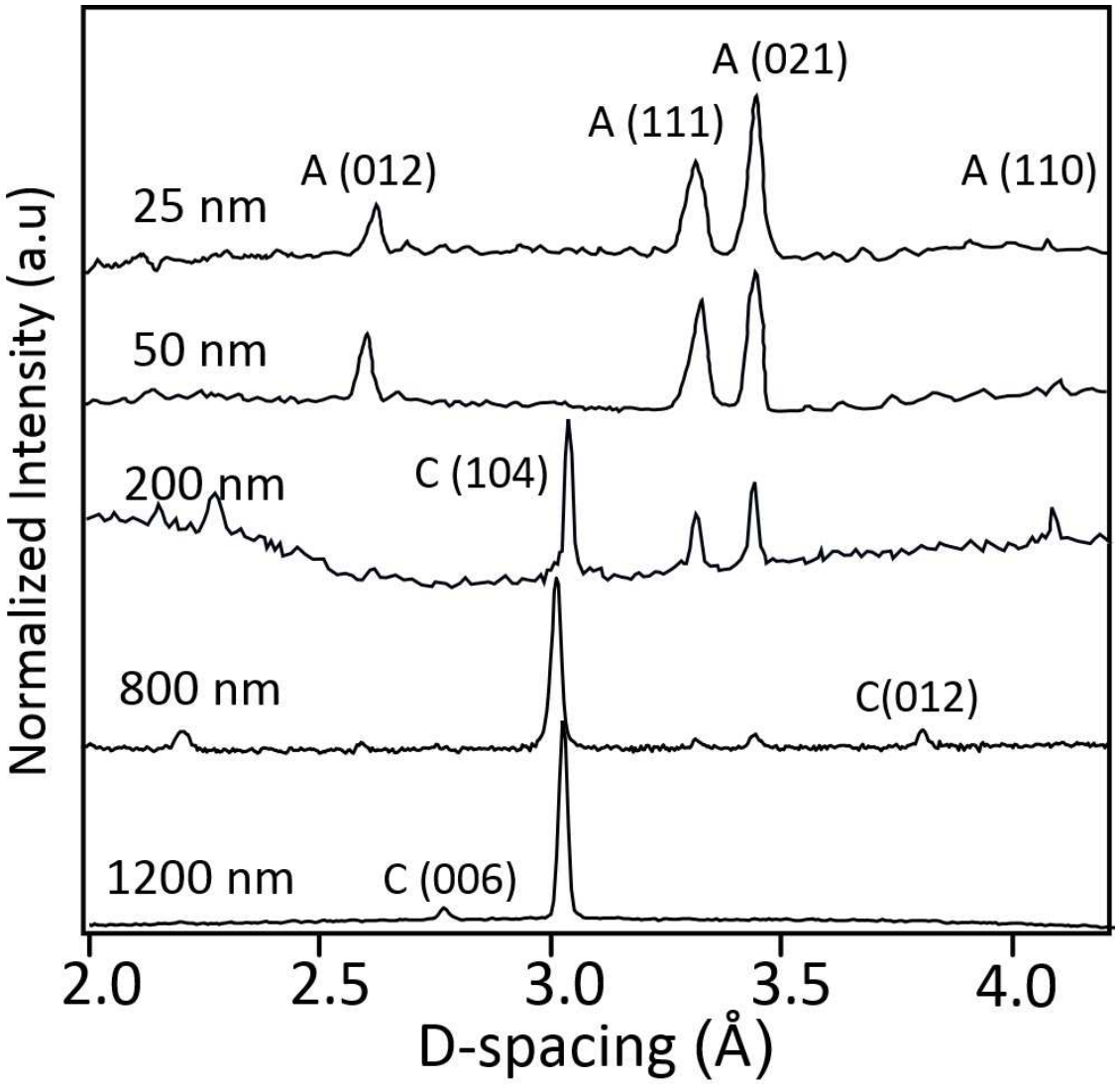

Figure 2: XRD spectra showing the increase in the proportion of aragonite formed as the pore size reduces for crystals precipitated under conditions $[Ca^{2+}] = [CO_3^{2-}] = 1.5$ mM and $[Ca^{2+}]$: $[Mg^{2+}]$: $[SO_4^{2-}] = 1: 2: 1$ (A: aragonite; C: calcite). Slight Shift of calcite reflections was due to Mg incorporation in calcite

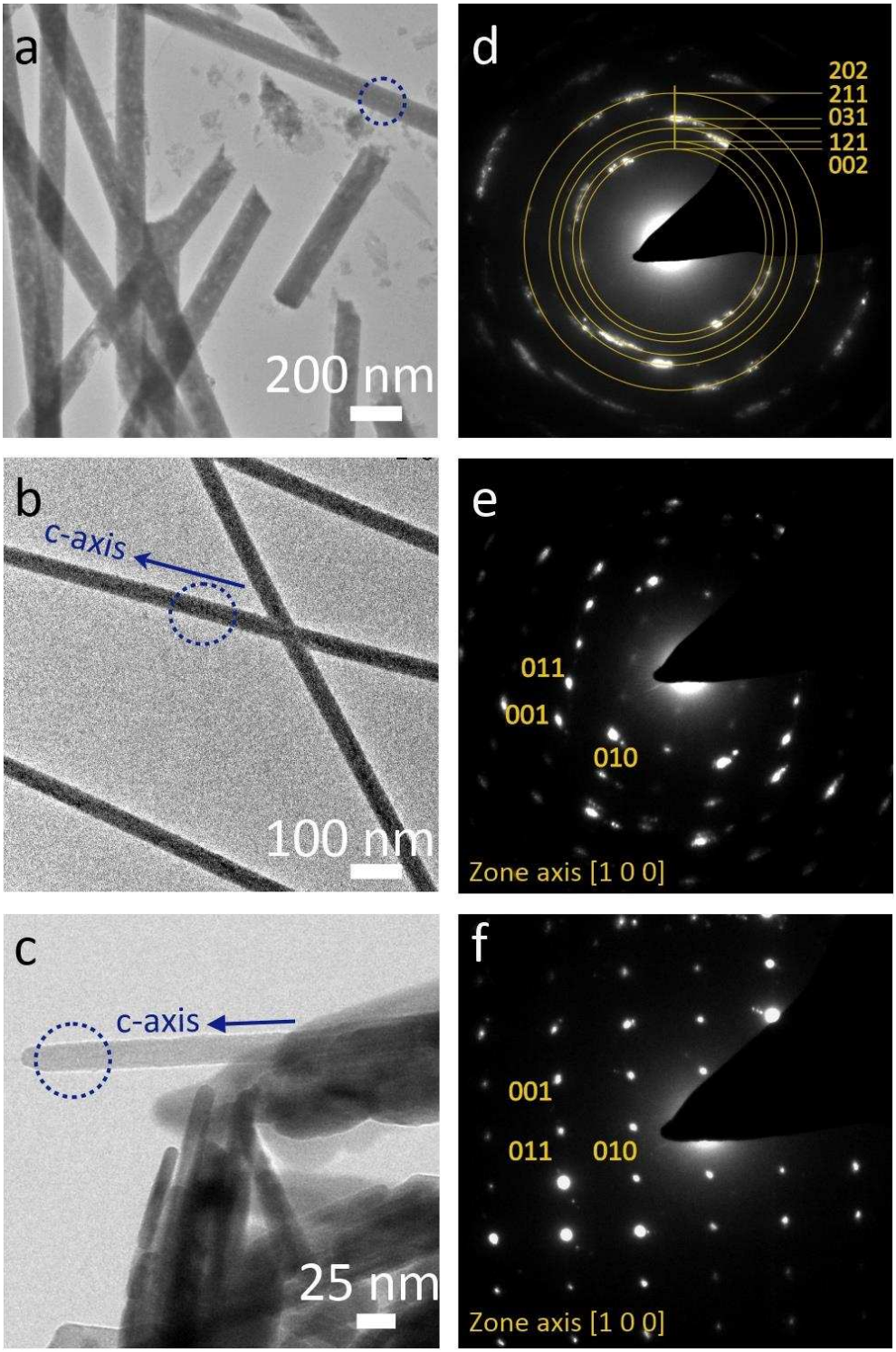

Figure 3. TEM images and electron diffraction patterns of rods precipitated from solutions of composition $[Ca^{2+}] = [CO_3^{2-}] = 1.5$ mM and $[Ca^{2+}]$: $[Mg^{2+}]$: $[SO_4^{2-}] = 1$: 2: 1 within (a) 200 nm, (b) 50 nm and (c) 25 nm pores. All patterns are indexed to aragonite.

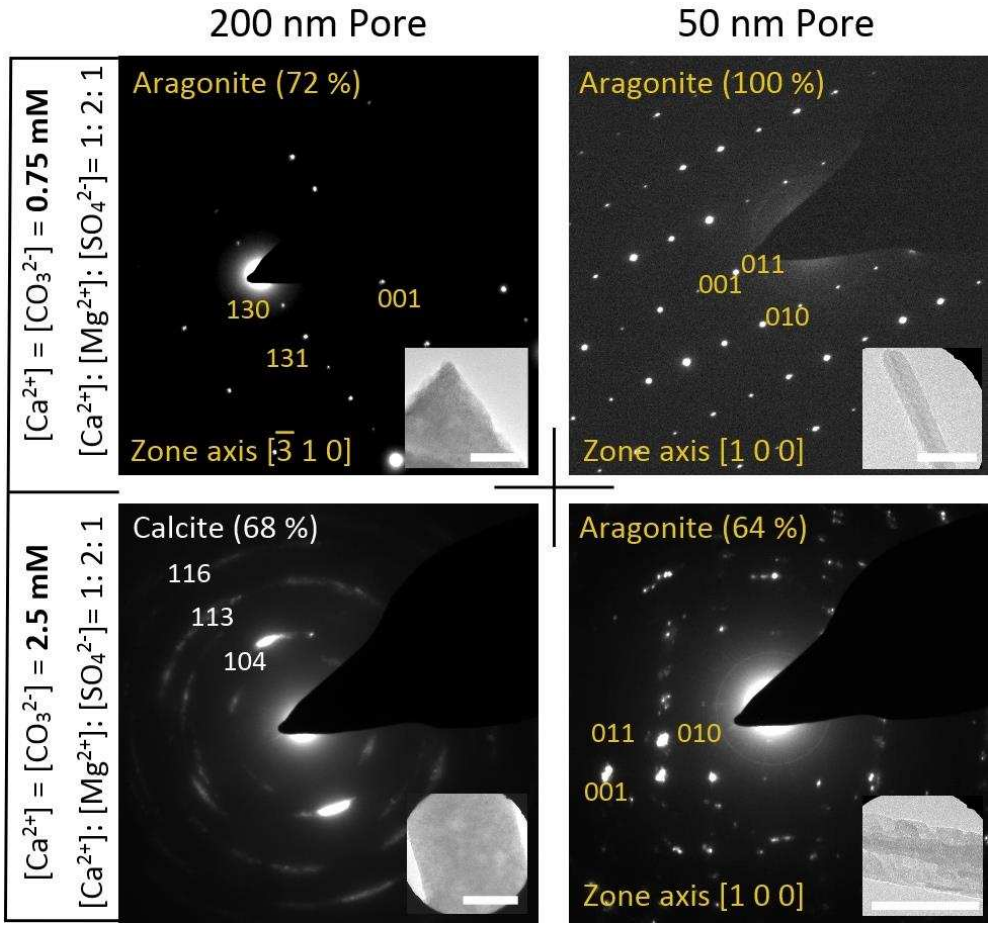

Figure 4. Influence of the calcium ion concentration on crystals precipitated within 200 nm and 50 nm membrane pores under reaction conditions of $[Ca^{2+}]$: $[Mg^{2+}]$: $[SO_4^{2-}]$ = 1: 2: 1. SAED patterns and corresponding TEM images (insets) of the polymorphs indicated are shown, together with the abundance of each polymorph under the given reaction conditions. The lowest supersaturation gives rise to single crystal aragonite in both the 50 nm and 200 nm pores. Scale bars are 100 nm.

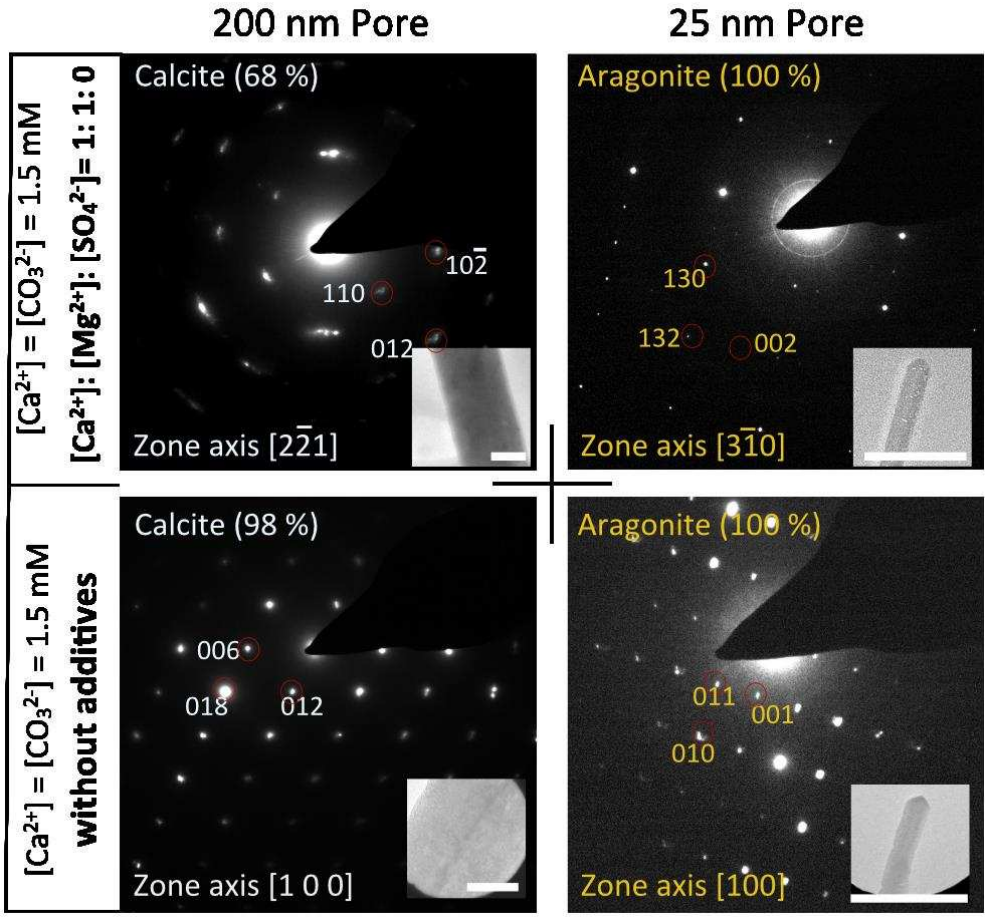

Figure 5. Influence of magnesium and sulfate ions on crystals precipitated within membrane pores under reaction conditions of $[Ca^{2+}] = [CO_3^{2-}] = 1.5$ mM. SAED patterns and corresponding TEM images (insets) of the polymorphs indicated are shown, together with the abundance of each polymorph under the given reaction conditions. Scale bars are 100 nm.

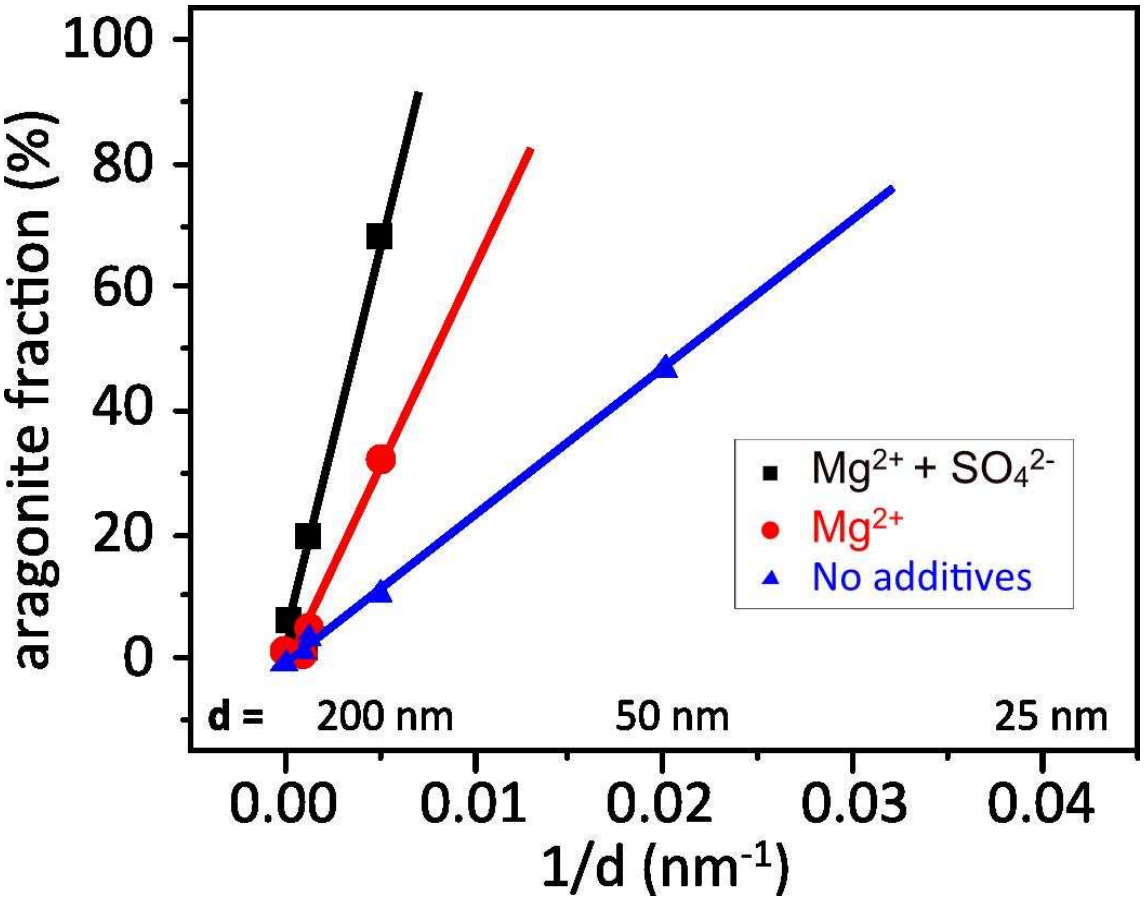

Figure 6. Mole percentage aragonite precipitated in pores of diameter d against 1/d at [$CaCO_3$] = 1.5 mM without additives and with additives as listed Table 1. The lines are least-squares fits with the points at 100% aragonite excluded, because the limited number of pore diameters does not enable us to determine exactly when 100% aragonite is attained. Errors in pore diameter (measured from TEM micrographs) and aragonite percentage are within the size of the symbols, except for the 25 nm pores, where the SEM results give values in the range $0.05 < 1/d < 0.067$, which has no effect on the fits. 100% aragonite samples are not shown as we do not know the precise pore size at which this would be achieved.

Supporting Information

Confinement Generates Single Crystal Aragonite Rods at Room Temperature

Muling Zeng, Yi-Yeoun Kim, Clara Anduix-Canto, Carlos Frontera, David Laundy, Nikil Kapur, Hugo K. Christenson and Fiona C. Meldrum

Experimental Methods

Chemicals and Materials: $CaCl_2 \cdot 2H_2O$, $MgCl_2 \cdot 6H_2O$, Na_2CO_3, Na_2SO_4 and dichloromethane were purchased from Sigma Aldrich and were used as received. Polycarbonate track-etched membranes with 200, 50 and 25 nm pores were obtained from ipPORE^{TM} (it4ip, Belgium), while membranes with pores sizes of 1200 and 800 nm were purchased from ISOPORE^{TM} (Merck Millipore Ltd, Ireland). The density and thickness of the membranes supplied by ipPORE are $\approx 4 \cdot 10^9$ pores cm^{-2} and 20 μm respectively, and from Millipore $\approx 4 \cdot 10^8$ pores cm^{-2} and 20 μm. Error in pore diameter of the membranes were measured by SEM and calculated: 1114 ± 49 nm, 799 ± 24 nm, 205 ± 10nm, 48 ± 3 nm and 20 ± 5 nm. Deionised water (Milli-Q Standard, resistivity = 18.2 MΩcm) was used in the preparation of the reactant solutions.

Precipitation of $CaCO_3$ within Track-Etched (TE) Membranes: Membranes were transferred to glass vials containing 15 mL of DI water and were degassed under reduced pressure to remove air from the pores. The membranes were then placed between two half U-tube arms, one of which was filled with a solution of $CaCl_2 \cdot 2H_2O$ and $MgCl_2 \cdot 6H_2O$, and the other with a solution containing Na_2CO_3 and Na_2SO_4. Crystallization was typically allowed to proceed for 2 days before the intra-membrane materials were extracted. After isolation from the U-tube system, the membranes were rinsed with DI water and ethanol and any crystals on the surfaces of the membranes were removed by scraping with a glass cover slide.

The intra-membrane particles were then isolated by dissolution of the membranes in dichloromethane. Membranes were transferred to centrifuge tubes filled with 1.5 mL dichloromethane, briefly sonicated and subsequently centrifuged for 8 mins at 15,000 rpm. Finally, the supernatant solution was removed and the dissolution-centrifugation cycle was repeated 3 further times, followed by washing in ethanol. In preparation for further analysis,

the precipitates were then re-dispersed in ethanol and pipetted onto either glass cover slides for examination by SEM, or TEM grids for investigation using TEM.

***Calcium Carbonate Precipitation in Bulk Solution*:** Control experiments were also performed by precipitating $CaCO_3$ in bulk solution under the same solution conditions used for the membrane experiments, where 5 mL volumes of the anion and cation solution were combined. The shape and sizes of the crystals were determined using Optical microscopy and Scanning Electron Microscopy (SEM) and the polymorphs were confirmed using PXRD and Raman microscopy. Each experiment was repeated 3 times to give enough material for PXRD.

Characterization

The morphologies of the $CaCO_3$ crystals precipitated in bulk solution on glass slides were visually examined using a Nikon Eclipse LV 100 optical microscope operated in transmission mode. SEM images were recorded with a FEI Nova Nano SEM 450. Prior to their examination, the substrates supporting the precipitates were attached to Al stubs holders with adhesive carbon pads and were coated with 2 nm Ir using an Agar high resolution sputter coater. Transmission Electron Microscopy (TEM) and selected area electron diffraction (SAED) were performed using an FEI Technai TF20 FEGTEM operating at 200 kV. The instrument was equipped with a Gatan Orius SC600A CCD camera. Samples for TEM were prepared by placing a drop of an ethanol suspension of the $CaCO_3$ rods onto a Cu TEM grid coated with Formvar and evaporated carbon. Raman microscopy was carried out using a Renishaw 2000 inVia instrument equipped with a 785 nm diode laser. A 50 $\times$ objective was used to focus the laser on the sample and spectra were typically recorded in the wavenumber range of 100 - 1200 cm^{-1} at 0.1 % laser power.

Samples for powder XRD were prepared by isolating the $CaCO_3$ precipitates from a fully dissolved membrane as described above. PXRD was performed using a Phillips X'Pert or a Bruker D8 Advanced diffractometer equipped with an X-ray source emitting Cu$K\alpha$ radiation. Samples were placed on a piece of corundum wafer and XRD data were collected in an angular range from 20 to 45° in intervals of 0.02°, with a scan rate of 1° min^{-1}. Phase quantification analysis was carried out by Rietveld analysis using X'Pert HighScore Plus software. Due to limited amounts of intra-membrane samples, we estimate 5-10% errors in the analysis. The

rods formed in smaller pores (25 and 50 nm) were collected and mounted on the holder for synchrotron XRD measurements, as too little material was available for powder XRD.

A number of samples (those precipitated in pores sizes of 50 nm and 25 nm) could not be isolated in sufficient quantities for analysis using laboratory PXRD and were there analyzed using synchrotron micro-beam XRD (μ-XRD). Measurements were performed on beamline B16 at Diamond Light Source, Oxford, UK. The beam-line produced a monochromatic beam of photons with an energy of 14.965 keV (0.8285 Å) and the focused X-ray beam size was 3.2 × 2.0 μm full width at half maximum (FWHM). Each sample was mounted in the loading device in the vertical plane (designated x-y in the laboratory coordinate system), with the incident beam travelling along the z-axis perpendicular to the sample. In order to locate the samples and calibrate the sample-to-detector distance and beam centre, a Si reference sample is used. The use of a monochromatic beam produces standard Debye-Scherrer diffraction rings that was converted into 1D intensity vs. D-spacing (Å)/ 2 Theta (^{o}) pattern using the FIT2D program.

The 1D diffraction patterns were analyzed by Rietveld analysis using FullProf. The determination of aragonite/calcite is difficult because the images recorded show discontinuous rings and single spots. For this reason, two different procedures were followed. The first method consisted of obtaining a powder diffraction pattern from the image, and fitting it by the Rietveld method. For this, we used a multiaxial March-Dollase description of the preferred orientation (as implemented in FullProf). As a second method, we directly extracted the integrated intensities found at every value of 2Θ from the image. Extracted intensities (for both polymorphs) were compared with the square of the corresponding structure factor to obtain an effective scale factor for every reflection for both aragonite and calcite. The average scale factors (made over the reflections with significant predicted intensity) were used for semi-quantitative analysis, giving a fraction of aragonite. The rationale behind this second method is that every spot in the image is created by a certain volume of the corresponding phase. The volume creating every spot can be estimated by the ratio between the spot's intensity and the square of the structure factor. The diffraction image sees the contribution from all these volumes. Averaging the ratio between intensity and the square of the structure factor corrects the probability that the existing volumes have the right orientation for contributing to the image.

Modelling Ion Diffusion through Membrane Pores

The diffusion equation was solved in a 2-dimensional axisymmetric co-ordinate frame, to capture the pore geometry with minimum computational effort. The diffusion equation can be expressed generally as:

$$\frac{\partial c_i}{\partial t} = D_i \nabla^2 c_i$$

where D_i and c_i are the diffusion coefficient and concentration of species i, respectively and t represents the time.

Boundary conditions along the surface of the membrane and walls of the pore are set as:

$$\frac{\partial c_i}{\partial n} = 0$$

where n is the outward facing normal. Unlike the case of the non-slip condition applied in the presence of fluid flow, the wall boundary allows motion of ions directly next to and parallel to the wall, hence the flat diffusion profile across the pore diameter. Along the fluid boundary, conditions are specified by fixing the concentration, which recognises the fact that the fluid domain either side of the membrane is effectively infinite, i.e. the number of ions transported across the membrane over the course of the experiment is small when compared to the initial number of ions of the species either side of the membrane. The diffusion equation is subject to the boundary conditions described above and shown in Figure S9, and is solved using the finite element method within Comsol Multiphysics. Initially, the concentration of the two species is set to zero within the pore. Due attention is paid to meshing of the high aspect ratio geometry to ensure grid-independent solutions. Our analysis also shopws that there is little change in the concentration of ions in the reservoirs over time, as their volume is large as compared with the membrane pores.

Figure S8 shows a series of snap-shots of the evolving concentration field for two species, Ca^+ and CO_3^{2-} (each with a diffusion coefficient of 0.8 x 10^{-9} m^2/s) with the concentrations of the two species scaled between 0 and 1. The analysis is conducted for 25 nm adn 1200 nm pores and demonstrates the insensitivity of concentration field to the pore diameter.

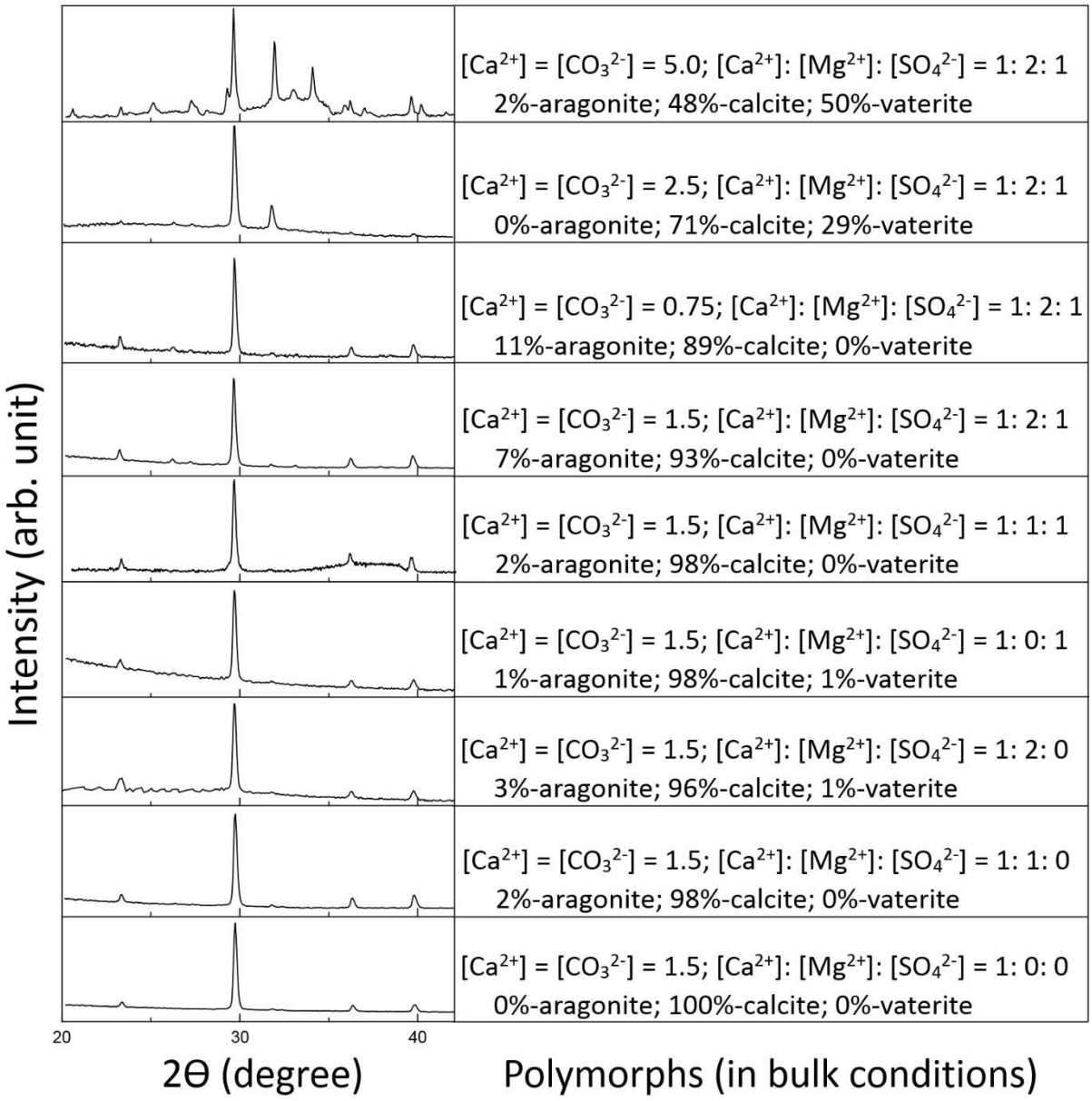

Figure S1. PXRD analysis of calcium carbonate polymorphs generated in bulk solution. The PXRD diffratograms are presented on the left of the diagram, while the corresponding analyzes are presented on the right hand side.

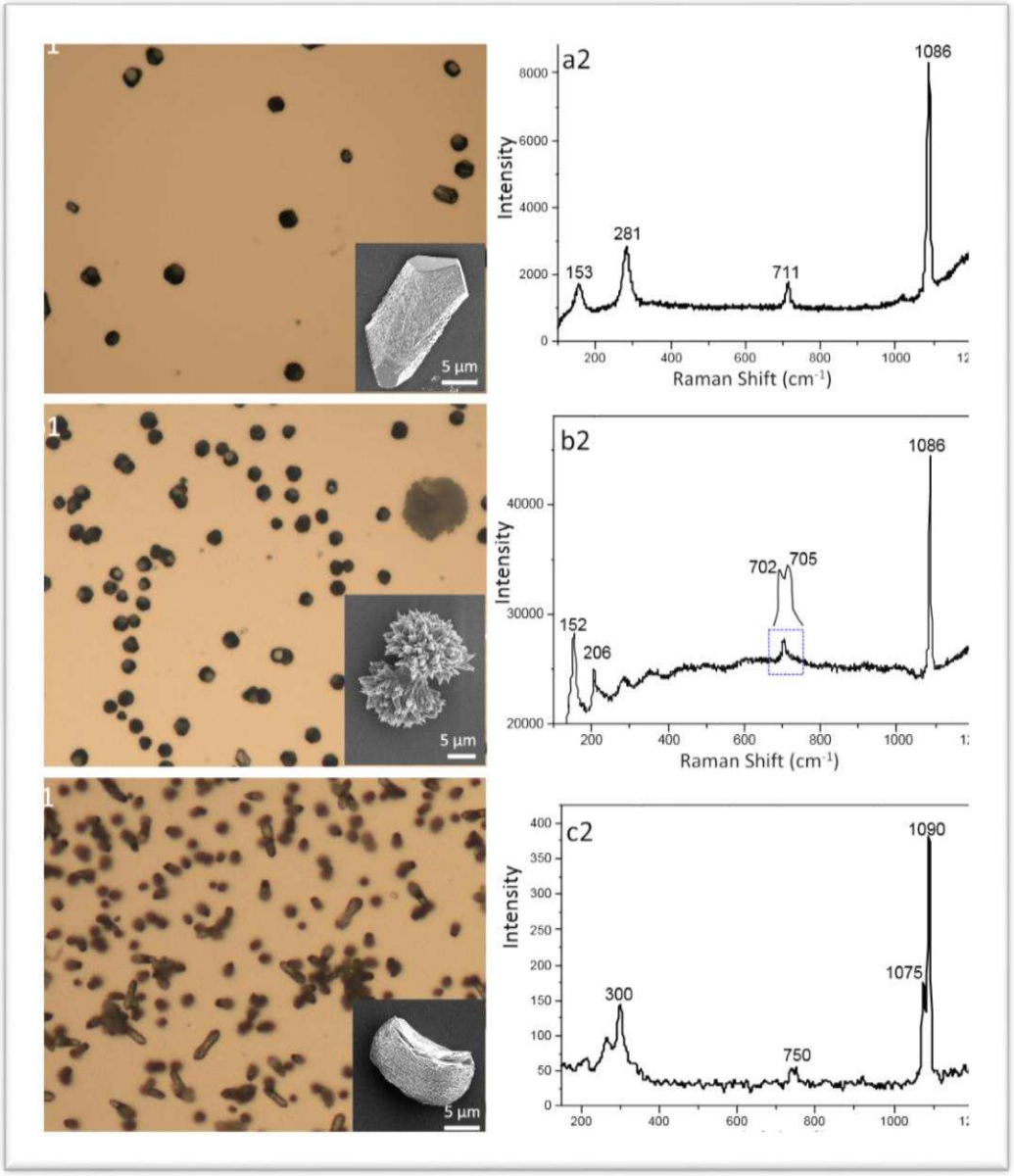

Figure S2. Optical and SEM images with corresponding Raman spectra of $CaCO_3$ crystals generated in bulk solution. (a1) Calcite crystal generated under "standard" conditions of $[Ca^{2+}] = [CO_3^{2-}] = 1.5$ mM and $[Ca^{2+}]$: $[Mg^{2+}]$: $[SO_4^{2-}] = 1$: 2: 1 and (a2) the corresponding Raman spectrum showing characteristic peaks at 1086 cm^{-1} (v1), 711 cm^{-1} (v4), 281 and 153 cm^{-1} (lattice modes). (b1) Aragonite crystal generated at $[Ca^{2+}] = [CO_3^{2-}] = 0.75$ mM and $[Ca^{2+}]$: $[Mg^{2+}]$: $[SO_4^{2-}] = 1$: 2: 1. (b2) Corresponding Raman showing characteristic aragonite peaks at 152 cm^{-1} and 206 cm^{-1} (lattice modes), 1086 cm^{-1} (v1) and a doublet at 702 and 705 cm^{-1} (v4). (c1) Vaterite crystal precipitated at $[Ca^{2+}] = [CO_3^{2-}] = 2.5$ mM and $[Ca^{2+}]$: $[Mg^{2+}]$: $[SO_4^{2-}] = 1$: 2: 1. (c2) Corresponding Raman spectrum showing characteristic double peaks at 1090 and 1075 cm^{-1} (v1).

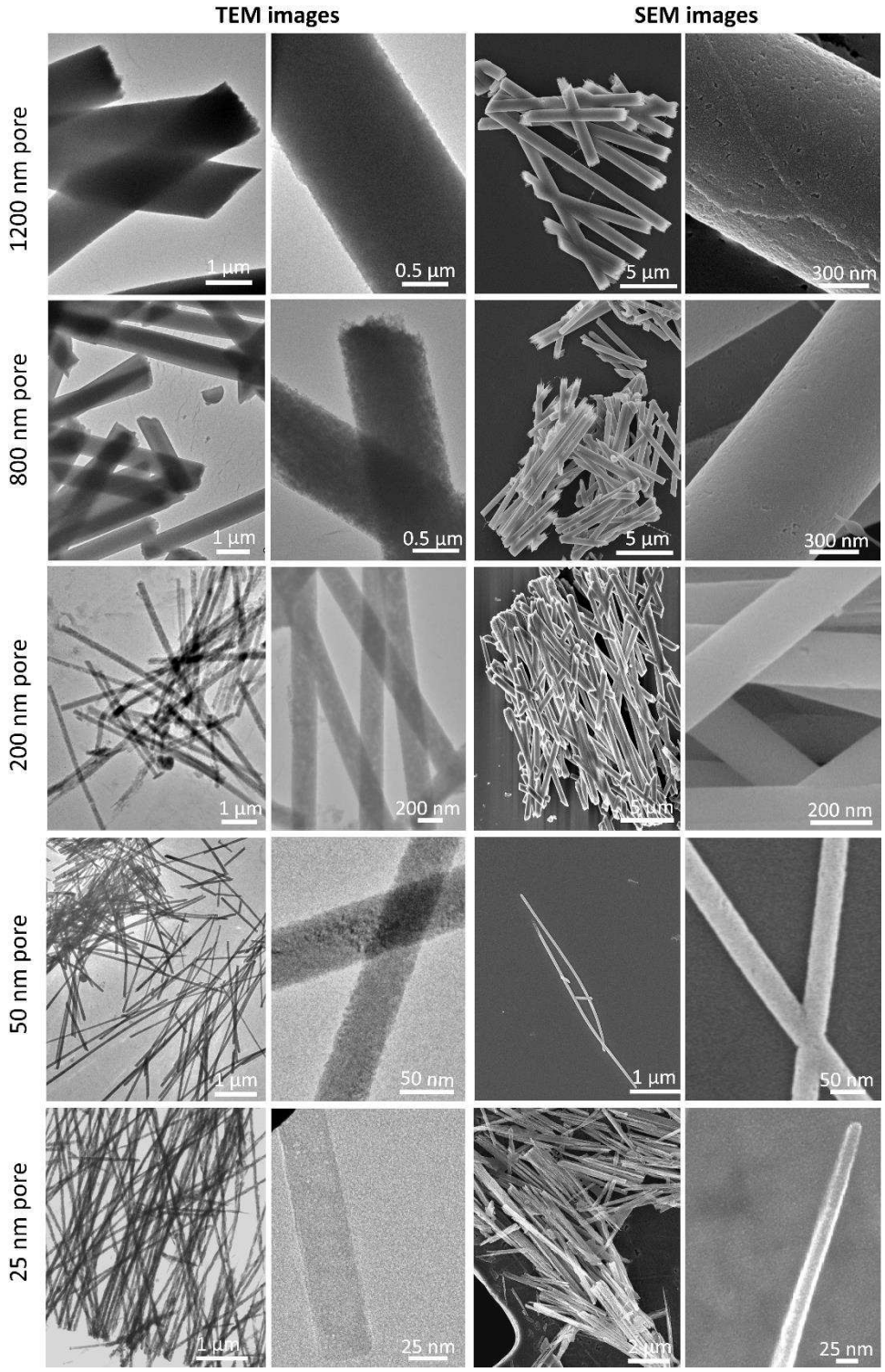

Figure S3. SEM and TEM images of $CaCO_3$ rods generated within TE membranes in the indicated pore sizes under "standard" conditions of $[Ca^{2+}] = [CO_3^{2-}] = 1.5$ mM and $[Ca^{2+}]: [Mg^{2+}]: [SO_4^{2-}] = 1: 2: 1$.

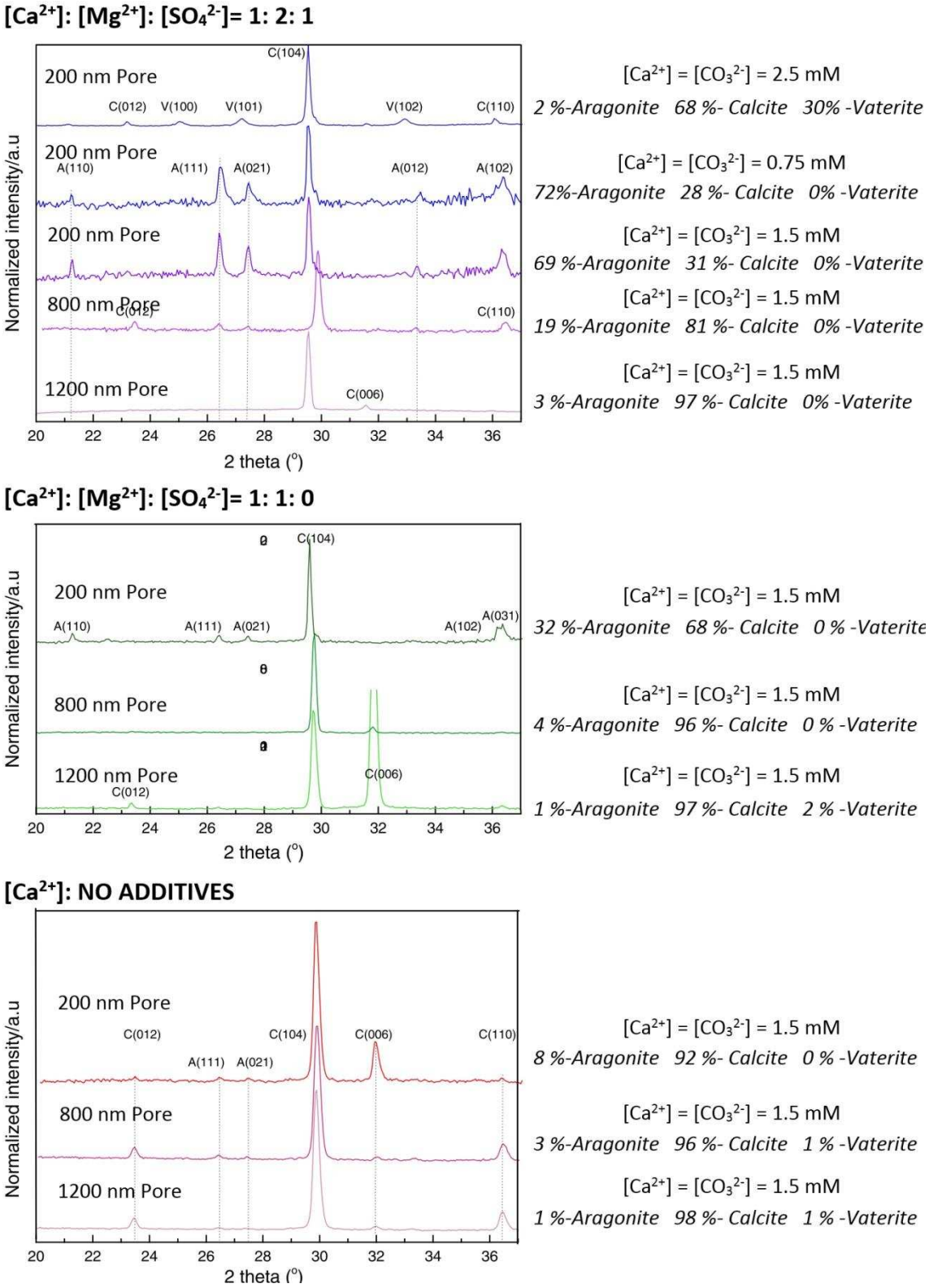

Figure S4. PXRD analysis of calcium carbonate polymorphs generated in the 1200, 800 and 200 nm pores of track etched membranes. The PXRD diffractograms are presented on the left of the diagram, while the corresponding analyses are presented on the right hand side.

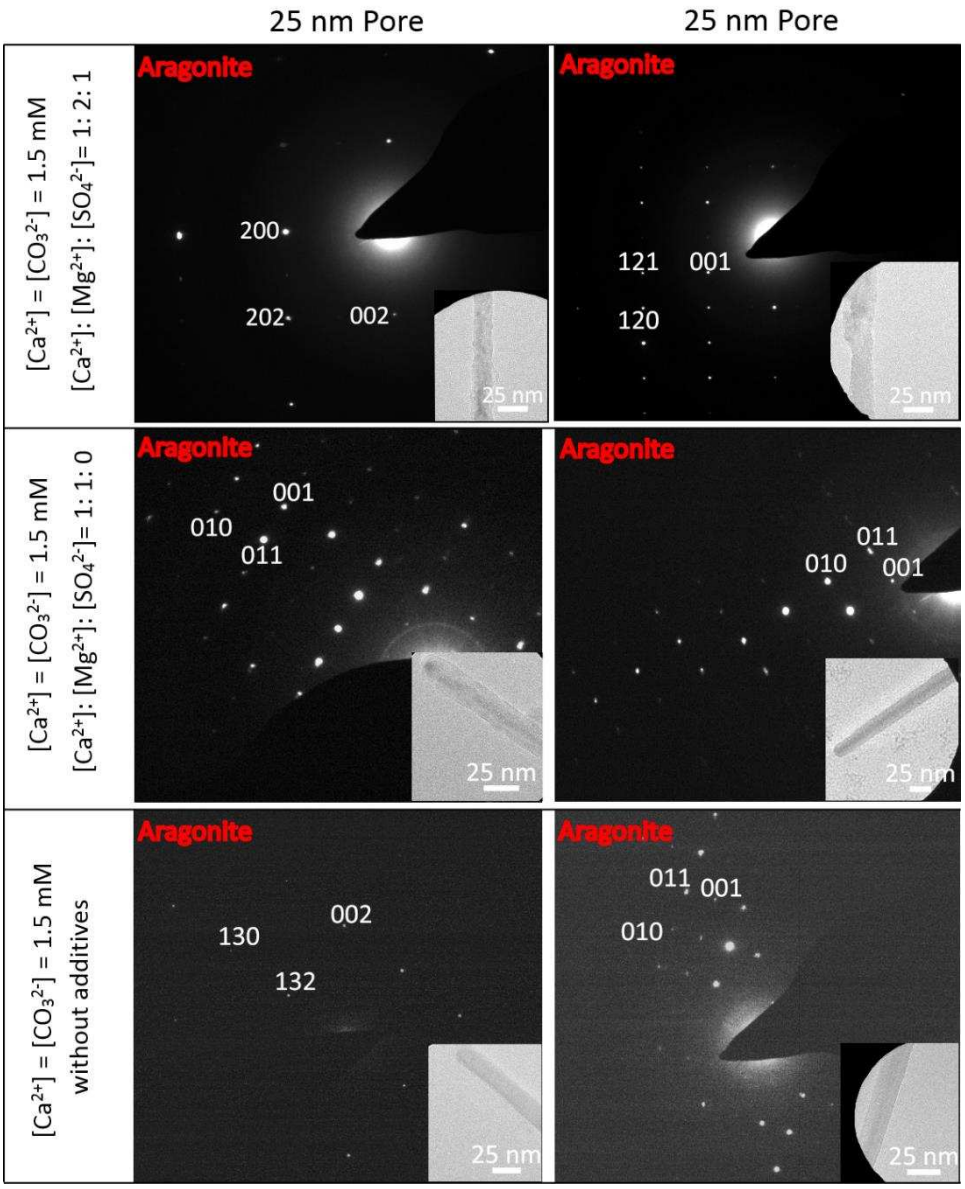

Figure S5. SAED patterns and corresponding TEM images of individual crystals precipitated within 25 nm pores under the reaction conditions indicated. The rods produced in the 25 nm pores were all single crystals of aragonite.

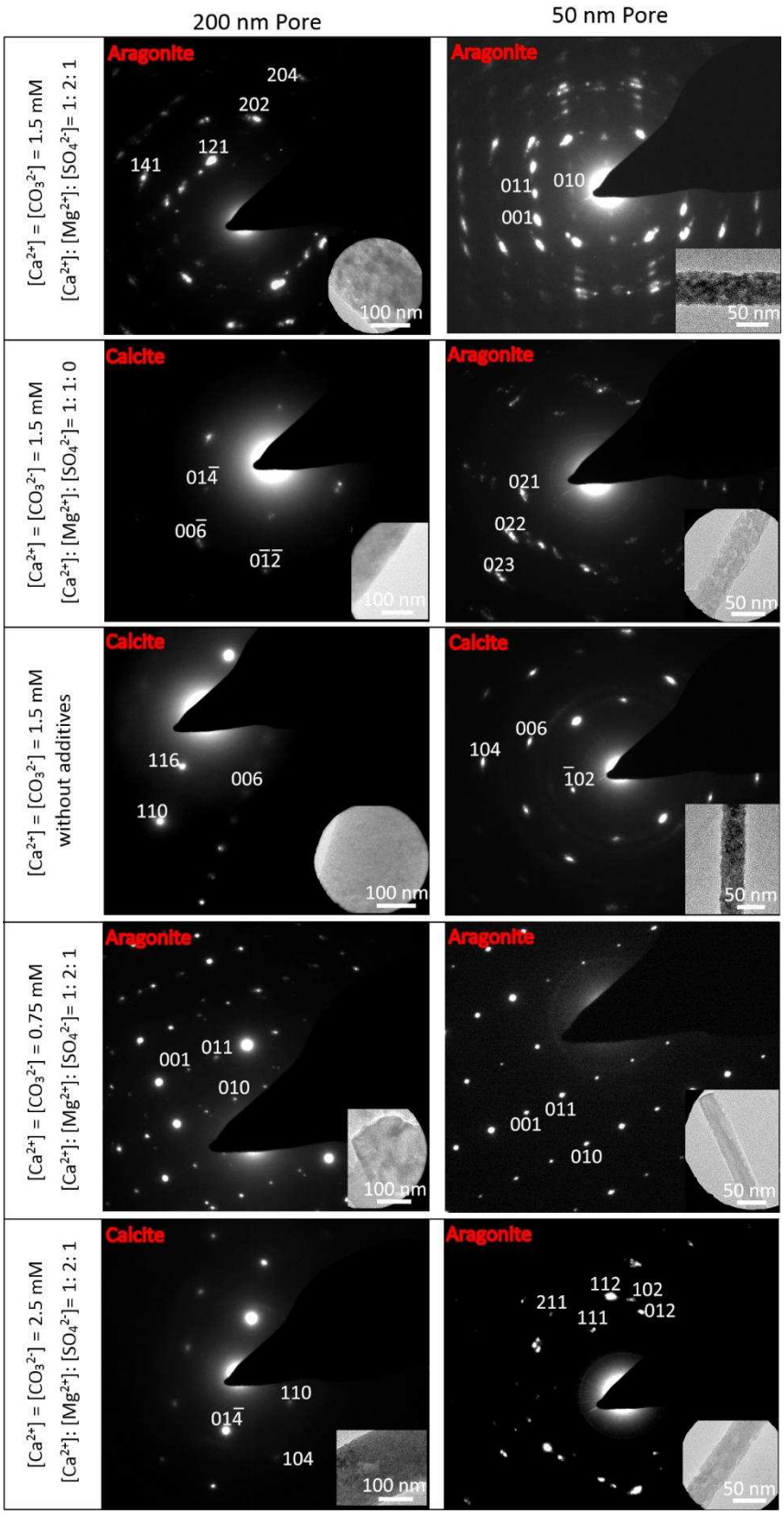

Figure S6. SAED patterns and corresponding TEM images of individual crystals precipitated within 200 and 50 nm pores under the reaction conditions indicated.

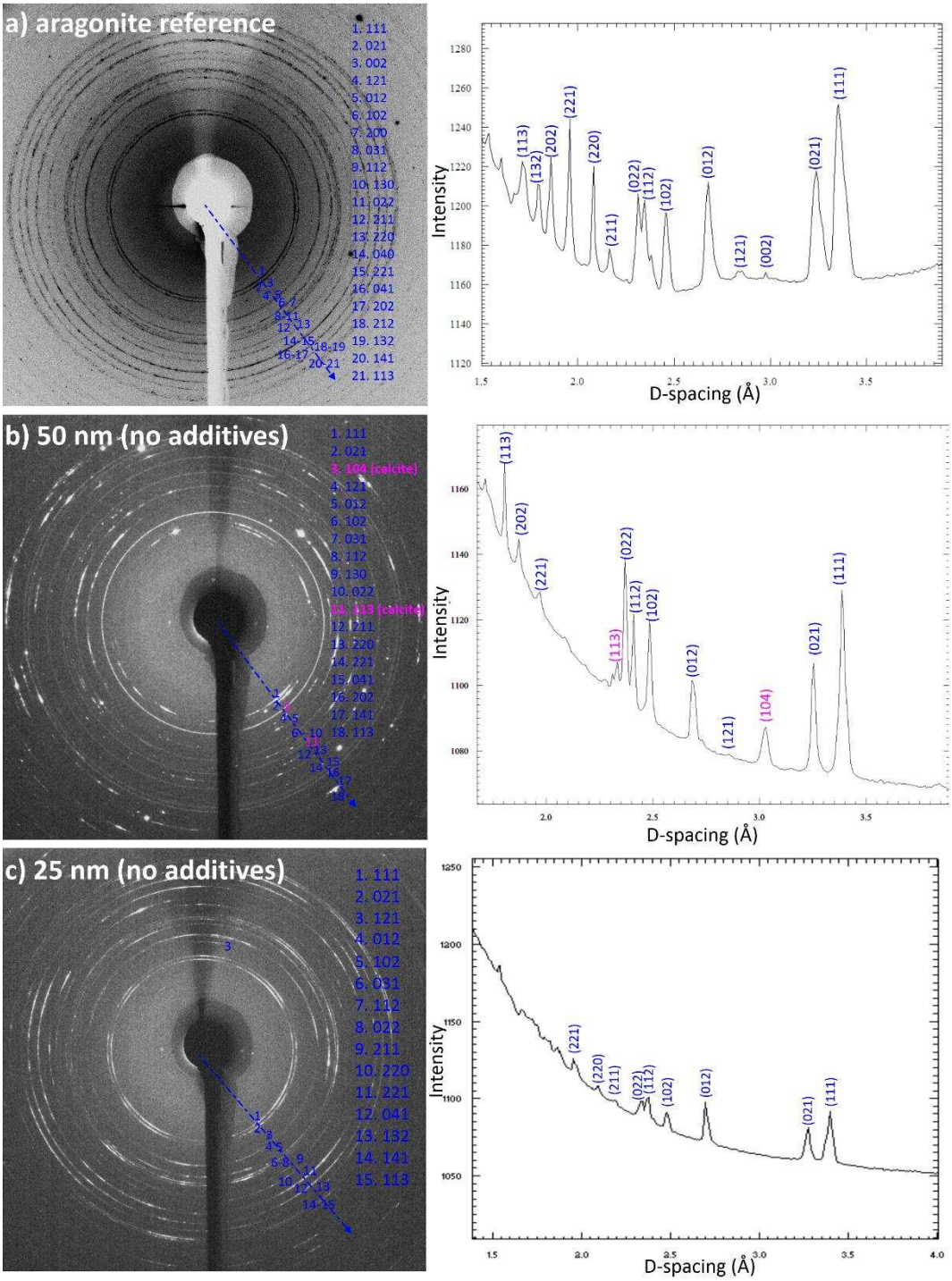

Figure S7. Synchrotron μ-XRD diffraction patterns: a) aragonite reference sample, b) crystal rods precipitated within 50 nm pores and c) 25 nm pores from the solutions of $[Ca^{2+}] = [CO_3^{2-}] = 1.5$ mM in the absence of any magnesium or sulfate. Original Debye-Sherrer rings are located on the left side, and their corresponding linear diffraction patterns are on the right side. The rest diffraction patterns from 50 and 25 nm (conditions of $[Ca^{2+}] = [CO_3^{2-}] = 1.5$, $[Ca^{2+}] :[Mg^{2+}] :[SO_4^{2-}] = 1: 2: 1$ and $[Ca^{2+}] = [CO_3^{2-}] = 1.5$, $[Ca^{2+}] :[Mg^{2+}] :[SO_4^{2-}] = 1: 1:0$) are similar to c) sample, which shown the peaks all belong to aragonite.

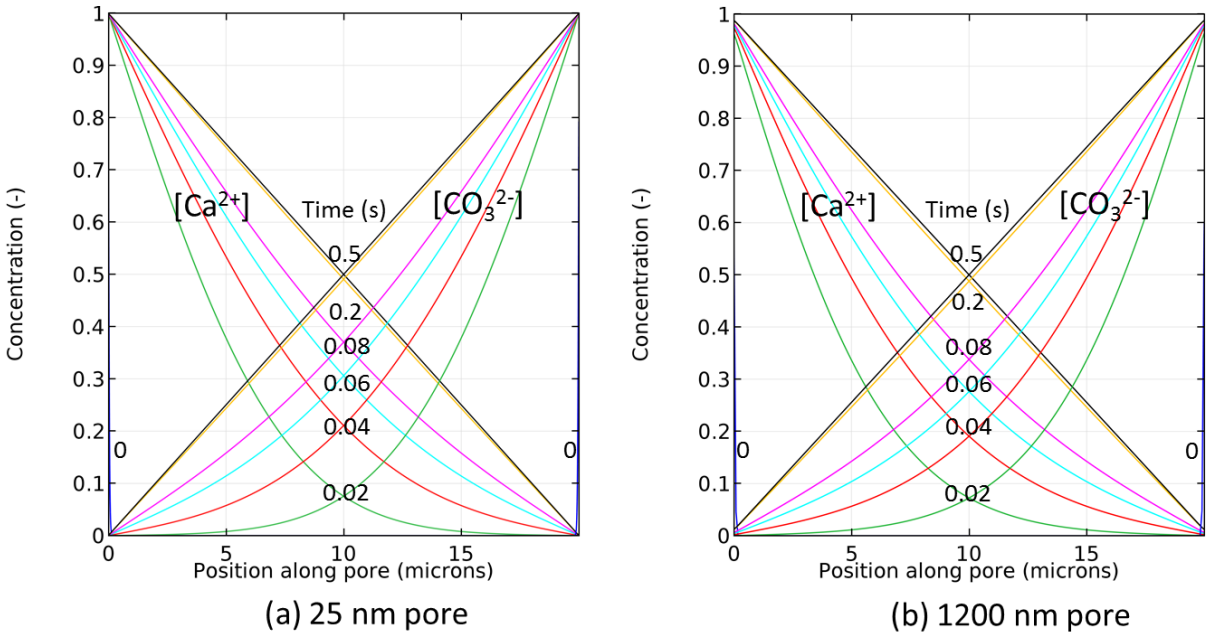

Figure S8: Concentrations of ions within a membrane pore of diameter (a) 25 nm (b) 1200 nm and length 20 µm as a function of time, as determined using COMSOL. The initial concentrations of ions are $[Ca^{2+}] = [CO_3^{2-}] = 1.5$ mM, and scaled between 0 and 1.

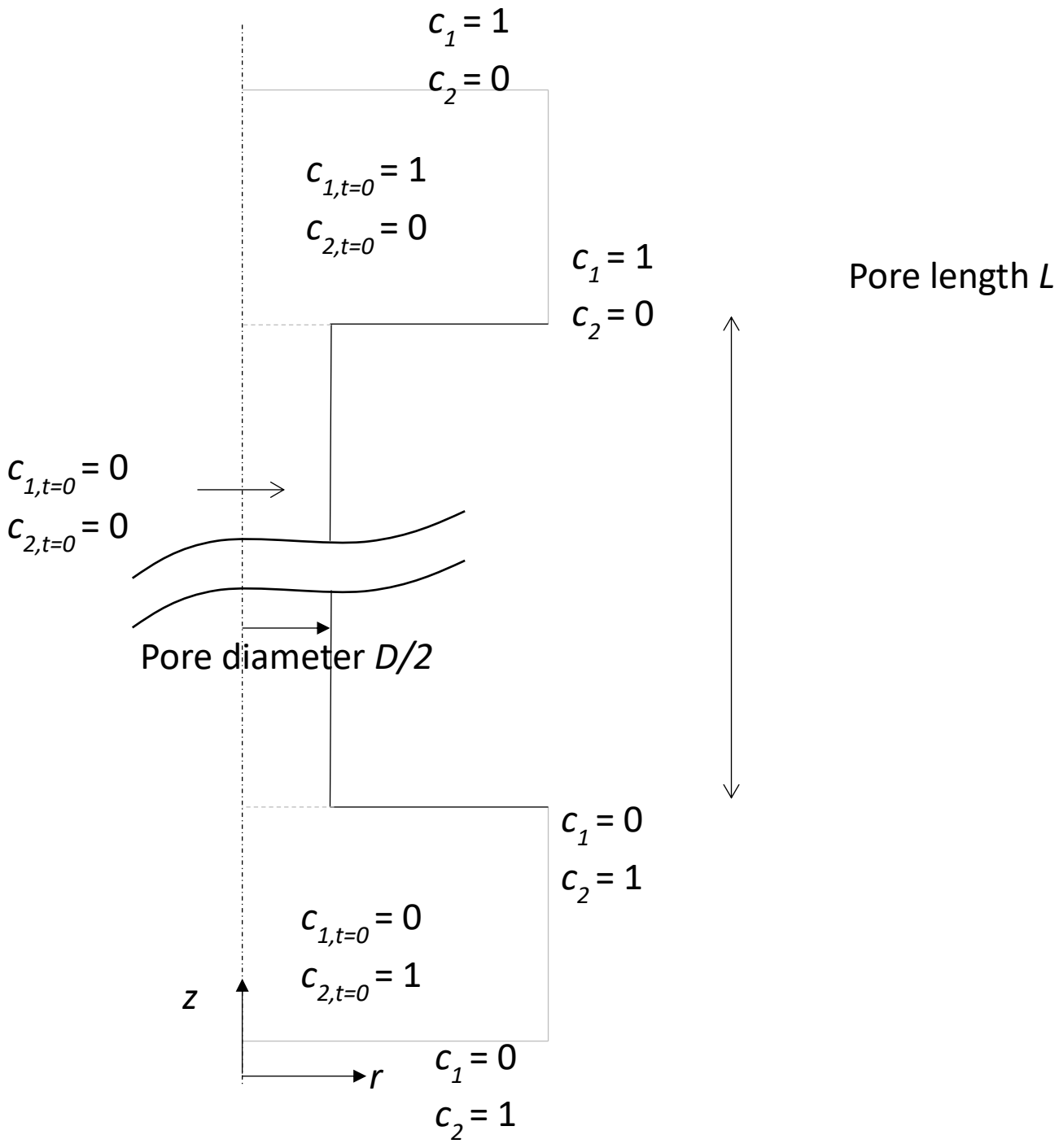

Figure S9. Initial and boundary conditions for the numerical simulation of ion transport across the membrane.